ACS APPLIED MATERIALS & INTERFACES

Research Article

www.acsami.org

Synthesis of Multifunctional Nanostructured Zinc–Iron Mixed Oxide Photocatalyst by a Simple Solution-Combustion Technique

Gajendra Kumar Pradhan, Satyabadi Martha, and K. M. Parida*

Colloids and Materials Chemistry Department, Institute of Minerals & Materials Technology (CSIR), Bhubaneswar-751013, Odisha, India

ABSTRACT: A series of nanostructure zinc–iron mixed oxide photocatalysts have been fabricated by solution–combustion method using urea as the fuel, and nitrate salts of both iron and zinc as the metal source. Different characterization tools, such as X-ray diffraction (XRD), X-ray photoelectron spectroscopy (XPS), diffuse reflectance UV–visible spectra (DRUV–vis), electron microscopy, and photoelectrochemical measurement were employed to establish the structural, electronic, and optical properties of the material. Electron microscopy confirmed the nanostructure of the photocatalyst. The synthesized photocatalysts were examined towards photodegradation of 4-chloro-2-nitro phenol (CNP), rhodamine 6G (R6G), and photocatalytic hydrogen production under visible light ($\lambda \geq 400$ nm). The photocatalyst having zinc to iron ratio of 50:50 showed best photocatalytic activity among all the synthesized photocatalysts.

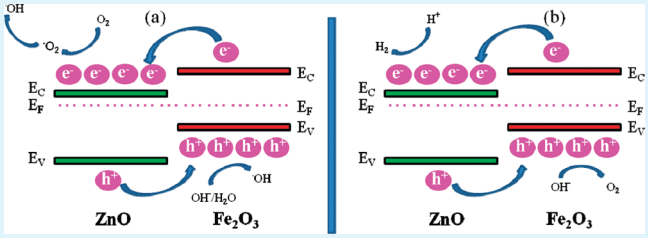

KEYWORDS: *nanostructure, mixed-oxide, solution-combustion, photocatalysis*

1. INTRODUCTION

As far as environmental problems and energy issues are concerned, scientists have paid a great deal of attention to the utilization of solar energy for the production of hydrogen from water and also degradation of organic pollutants using photocatalysts.[1,2] Hydrogen production from water using semiconductor photocatalysts have attracted considerable interest since the pioneering work of Fujishima and Honda.[3] Since then, various metal oxide semiconductor photocatalysts were studied towards water decomposition reaction for hydrogen production. But most of the materials were active under UV light irradiation.[4,5] More recently, attention have been paid for the development of photocatalysts that are capable of using visible light (λ = 400–700 nm) for the photocatalytic production of H_2. Although a large number of materials have been developed for production of hydrogen energy from water under visible light, still the efficiency is very low.[6,7]

Rhodamine 6G, phenol and its derivatives are highly carcinogenic and have adverse effect to the aquatic environment. Contamination of water by these compounds is a serious issue to the whole ecosystem.[2,8−13] Because dye and phenolic compounds are generated as effluents from various industries, it requires proper treatment prior to discharging into the environment. For the removal of phenol, various techniques such as ozonolysis, photosynthesis, photocatalytic decomposition, reverse osmosis, ion exchange, precipitation, and electrodialysis have been previously used.[14−16] Photo-fenton oxidation is another advanced process for the mineralization of various pollutants. So scientists are eager to resolve these issues to make the environment clean.

Metal oxide is the best choice for heterogeneous photocatalysis to eliminate various dyes, phenolic compounds, pollutants etc. Besides this, it may bring revolution to the world by solving the fuel crisis in near future. Iron oxide has been of special interest because of its high absorptive supremacy in the visible range. However the lower band gap ($\leq$ 2.2), electron-hole recombination limits its application towards photocatalysis. In order to address these issues, incorporation of heteroatom (e.g., Si, Bi, Pt, and Ta), quantum confinement and architectural control have been taken into consideration.[17−21] Band gap of ZnO is 3.1 eV as reported by many researchers which is transparent to the visible light and absorbing only UV light from the solar spectrum where only 5 % solar light is available.[22] On the other hand, the mixed oxides systems have the ability to obtain structures in combination with the properties that individual oxide doesn't possess. Coupling of two semiconductors (e.g., CdS/TiO_2, CdS/ZnO, TiO_2/SnO_2, CdSe/TiO_2) with suitable energetic can significantly improve the selectivity and enhance the charge-separation yield.[23−26] The combination of ZnO with Fe_2O_3 can be an efficient photocatalyst and can fulfil the seeking property of individual material.

Metal oxide nanoparticles have been synthesized by various techniques such as sol-gel, hydrothermal, precipitation, co-precipitation etc.[27−30] Among all, solution-combustion technique is another significant method having many advantages over others. It requires lesser time, generates high purity and highly

Received: September 27, 2011
Accepted: December 27, 2011
Published: December 27, 2011

crystalline products/materials.[31] Previously, we have studied hematite and titania systems for photocatalytic degradation of different dyes.[2,32] The present work highlights the synthesis and characterization of iron−zinc nanosized mixed oxide by simple solution-combustion method. Using the catalyst, we have studied the degradation of CNP and R6G by photofenton reaction. Also we have studied the H_2−Production from aqueous methanol solution under visible light. Overall, our synthesized photocatalysts are showing multifunctional activity.

2. EXPERIMENTAL SECTION

2.1. Materials. All the chemicals and reagents are of analytical grade and used without further purification. Iron(III) nitrate nonahydrate ($Fe(NO_3)_3.9H_2O$) (Acros organics), zinc nitrate hexahydrate ($Zn(NO_3)_3.6H_2O$) (Fischer Scientific), urea-(NH_2CONH_2) (Merck), and deionized water were used for the preparation of the sample. Rhodamine 6G (Acros) and 4-chloro-2-nitro-phenol (Aldrich) were used for degradation study.

2.2. Methods. The photocatalysts were synthesized by solution-combustion method by taking metal nitrate and urea as oxidant and fuel, respectively.[33,34] Predetermined quantity of respective nitrate salts of both iron and zinc were taken in distilled water followed by the addition of urea and was allowed to stir for 30 minutes. Pure iron oxide was prepared by taking only iron nitrate along with the fuel and is named as 0Zn. Similarly, pure zinc oxide was prepared from zinc nitrate and was named as 100Zn. Mixed oxides were prepared by maintaining the molar ratio of $Zn(NO_3)_3{\cdot}6H_2O/Fe(NO_3)_3{\cdot}9H_2O$, i.e., 10:90 (10Zn), 40:60 (40Zn), 50:50 (50Zn), 60:40 (60Zn), 90:10 (90Zn), respectively. Then the solution was transferred to a high-temperature resistant crucible and was kept for 5 min in the muffle furnace, which was previously maintained at 500 °C. After 5 min, the powder sample was taken out and allowed to cool. It was then collected, grinded, and calcined at 500 °C for 4 h. The whole synthetic procedure is shown in Scheme 1.

Scheme 1. Schematic Representation of Iron−Zinc Mixed Oxide Preparation

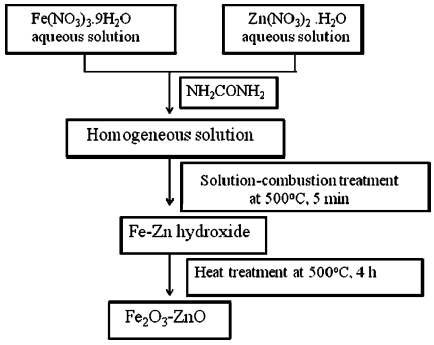

2.3. Characterization. Powder X-ray diffraction patterns of the samples were recorded in a PANalytical X-ray diffractometer using Ni filtered Cu Kα radiation (λ = 1.5418 Å). Transmission Electron microscope (TEM) of the catalysts were recorded with a model FEI, TECNAI G^2 20, TWIN, Philips operating at 200 kV. The particle size of all the photocatalysts were calculated by using ImageJ programme. Optical absorbance spectra of the catalysts were recorded using a Cary 100 spectrophotometer (Varian) in the spectral range of 200-800 nm. Boric acid was used as the reference. N_2 adsorption−desorption studies were performed at -197 °C in Automated Surface area and Porosity Analyser (ASAP 2020, Micromeritics, USA). Prior to the analysis, the samples were degassed under vacuum (1×10^{-5} Torr) at 300 °C for 4 h. The electronic states of Fe and Zn were examined by X-ray photoelectron spectroscopy (XPS, Kratos Axis 165 with a dual anode (Mg and Al) apparatus) using the MgKα source. All the binding energy values were calibrated by using the contaminant carbon (C1s = 284.9 eV) as a reference.

2.4. Photocatalytic Reaction. *2.4.1. Photocatalytic Degradation of CNP and R6G.* The photodegradation of both CNP and R6G were studied over all the synthesized catalyst. In a typical experiment, 20 mg (1g/dm^3) of catalyst in 20 mL of 100 ppm CNP (0.5 mmol) and R6G (0.2 mmol) solutions were taken in a 100 mL closed Pyrex flask. One microliter of 1×10^{-4} M H_2O_2 (0.1 mmol) was added to the above solution to enhance the photocatalytic efficiency of the catalysts. The photocatalytic reactions were performed using a pyrex flask with a water circulation facility at the outer wall of the reactor and with a specific outlet for the sample collection. The temperature of the reactor was kept constant at 30 °C for all photocatalytic reactions. The solutions were then exposed to the sunlight with constant stirring with a speed of 600 rpm for 4 h. The photocatalytic experiments were also carried out at different stirring speed such as 500, 550, and 600 rpm. But, the optimum result was obtained at 600 rpm and hence all the experiments were performed at 600 rpm. After irradiation, the suspension was centrifuged and the concentration of the supernatants was analyzed quantitatively using a Cary-100 (Varian, Australia) spectrophotometer. Degradation of CNP and R6G were monitored at wavelength of 280 and 532 nm, respectively. The presence of metal ions in the (leaching test) solution was determined by an atomic absorption spectroscopy (Perkin-Elmer Analysis 300) using acetylene (C_2H_2) flame. All photocatalytic experiments in this investigation were reproducible with ±3 % variation. Total organic carbon (TOC) removal was determined using a TOC Analyser, ANATOC series II.

We have measured the intensity of solar light by using Digital Illuminance Meter (TES-1332A, Taiwan) with inbuilt Si-diode. The sensor was always set in the position of maximum intensity and the solar light intensity was measured in every hour between 11:00 and 15:00. The average intensity of the solar light was found to be 100 000 lux.

2.4.2. Photocatalytic Hydrogen Generation. The catalytic activity and deactivation were studied in a batch reactor. About 0.05 g (1g/dm^3) of catalyst was suspended in 50 mL of an aqueous solution containing 10 vol % CH_3OH for H_2 evolution. The solution was kept under stirring with a magnetic stirrer, prohibiting particles from settling down at the bottom of the reactor. Prior to irradiation, the reaction mixture was purged with N_2 in order to remove the dissolved gases. A 125 W medium pressure Hg visible lamp was used as the source of light and 1M $NaNO_2$ solution is used as UV filter ($\lambda \geq 400$). The evolved gas was collected by water displacement technique and analyzed by GC-17A using 5 Å molecular sieve column with a thermal conductivity detector (TCD). A comparison of the retention time of the peaks that appeared on the chromatogram with standards confirmed that the gas was hydrogen.

3. RESULTS AND DISCUSSION

3.1. Formation of Metal Oxides and Mixed Metal Oxides. The formation of Fe_2O_3, ZnO, and $ZnFe_2O_4$ have been discussed in Scheme 2. Upon the addition of urea and water to the metal nitrates followed by heating, there is subsequent release of carbon dioxide, water, and nitrogen dioxide. This leads to the formation of metal oxides and mixed metal oxide depending upon their metal source.

Scheme 2. Formation of Metal Oxides and Mixed Metal Oxides

$$Fe(NO_3)_3.9H_2O + NH_2CONH_2 \longrightarrow Fe_2O_3 + CO_2 + H_2O + NO_2 \quad \text{.....(1)}$$

$$Zn(NO_3)_3.6H_2O + NH_2CONH_2 \longrightarrow ZnO + CO_2 + H_2O + NO_2 \quad \text{.....(2)}$$

$$Zn(NO_3)_3.6H_2O + Fe(NO_3)_3.9H_2O + NH_2CONH_2 \longrightarrow Fe_2O_3 + ZnO + ZnFe_2O_4 + CO_2 + H_2O + NO_2 \quad \text{.....(3)}$$

3.2. XRD. The XRD spectrum can be matched to the series of Bragg reflections corresponding to the standard JCPDS with

the observed diffraction peak (Figure 1). Both the diffraction peaks of 0Zn and 100Zn were assigned to its corresponding α-

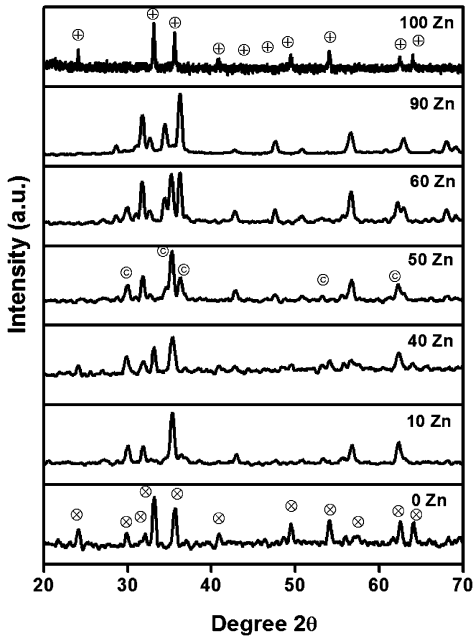

Figure 1. XRD patterns of 0Zn, 10 Zn, 40 Zn, 50 Zn, 60 Zn, 90 Zn, and 100 Zn photocatalysts (The symbols ⊗, ⊕, and © represents Fe_2O_3, ZnO, and $ZnFe_2O_4$, respectively).

Fe_2O_3 and ZnO phase, respectively (JCPDS File no.13-534, and 21-1486, respectively). However, with the increase in both Fe and Zn concentration, there is appearance of new peaks along with peaks of ZnO and Fe_2O_3. These new peaks are assigned to $ZnFe_2O_4$ (JCPDS File no. 1-1108) and the diffraction peaks of $ZnFe_2O_4$ get more intense in the ratio of 50:50 (50Zn). This infers the formation of mixed oxide of iron and zinc including its single phase of $ZnFe_2O_4$.

The percentage of each phase (Fe_2O_3, ZnO, and $ZnFe_2O_4$) were calculated from the highest intense XRD peaks. The percentage of a particular phase is given by

$$X(\%) = \frac{I_X}{1a + ab + 1c} \times 100 \quad (1)$$

where $X = a, b, c$, and $a = Fe_2O_3$, b = ZnO, $c = ZnFe_2O_4$. From the above equation, the percentage of Fe_2O_3, ZnO, and $ZnFe_2O_4$ were found to be approximately 26, 22, and 52, respectively.

3.3. Electron Microscopic Study. TEM images were taken to elucidate the morphology of the samples. Figure 2a displays the typical TEM images of the as-synthesized photocatalyst. The particle size of all the photocatalysts were shown in Table 1. The particle size of all the samples is varied in the range of 33−55 nm. Among all, 50Zn shows lowest particle size and the average size was found to be 37 ± 8 nm. For better understanding, we have also carried out HRTEM measurements of 50 Zn sample. The HRTEM image of 50 Zn sample is presented in Figure 2b. From HRTEM, it was observed that the mixed oxide nanoparticles exhibit lattice fringes with interplanner spacing 2.54 Å assigned to 311 plane of $ZnFe_2O_4$. We have also observed that the lattice fringes of 2.47 and 2.70 Å, which correspond to interplanner spacing of 101 and 104 planes of ZnO and Fe_2O_3 of 50Zn sample. Thus

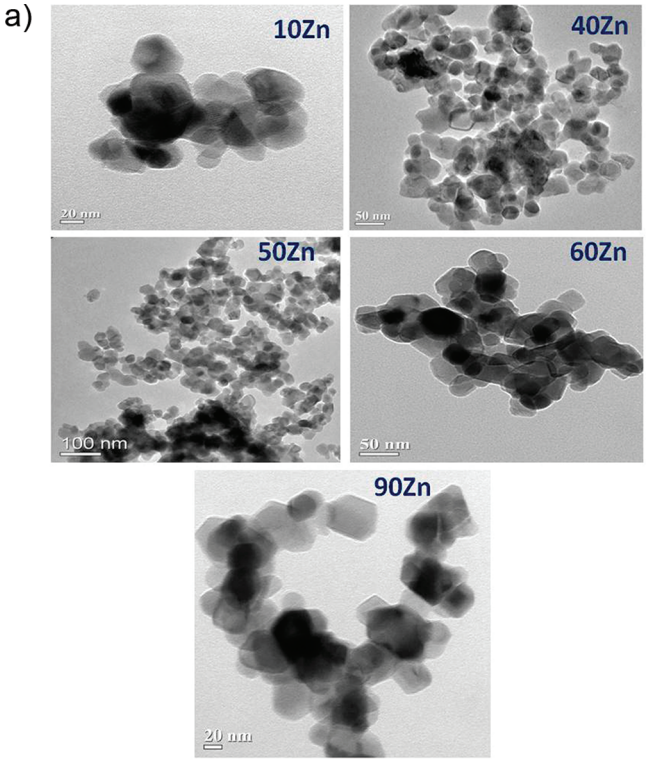

Figure 2. (a) Representative TEM images of 10 Zn, 40 Zn, 50 Zn, 60 Zn, 90 Zn. (b) HRTEM of 50Zn photocatalyst.

the HRTEM image of 50Zn confirmed the formation of highly crystalline material with three distinct phases of ZnO, Fe_2O_3, and $ZnFe_2O_4$.

3.4. DRS. Diffuse reflectance spectra of 100Zn, 0Zn, and 50Zn samples were presented in Fig. 3. 100Zn exhibits its absorbance band at 383 nm whereas the observed band for 0Zn at 399 nm due to direct charge transfer transitions from O^{2-} 2p to Fe^{3+} 3d ($^6A1 \rightarrow {}^4T_2$). The band gap observed for 0Zn, 50Zn and 100Zn were 2.0, 2.19, 3.19 eV respectively as calculated. Also the finger print region of the band edge of hematite is 521−-565 nm and in our 0Zn sample shows its band edge from 540−577 nm.[35] On the other hand, the band edge for 0Zn is observed in the region of 372-394 nm in the spectrum. However, for 50Zn, where equal percentage of both Fe and Zn are present exhibits its band edge in the range of 467-534 nm. This band edge is red shift of ZnO (100Zn) and blue shift of Fe_2O_3 (0Zn). So it shows the property in between 0Zn and

dx.doi.org/10.1021/am201326b | ACS Appl. Mater. Interfaces 2012, 4, 707−713

Table 1. Surface Properties, Photodegradation of 4-Chloro-2-nitro Phenol (CNP) and Rhodamine 6G (R6G), Hydrogen Evolution, 0.1 mmol of H_2O_2, 0.5 mmol of CNP, and 0.2 mmol of R6G, 1g/dm^3 of Catalyst, Reaction Time 4 h

					% of degradation		
sample name	particle size (nm)	surface area (m^2/g)	pore volume (cm^3/g)	pore diameter (nm)	CNP	R6G	hydrogen evolution (μmol/h)
0Zn					21 ± 1	41 ± 3	
10Zn	44 ± 5	8.8	0.094	40.7	33 ± 2	58 ± 3	99.4
40Zn	41 ± 4	16.5	0.166	41.4	45 ± 2	72 ± 1	138.9
50Zn	37 ± 8	17.7	0.17	43.8	56 ± 2	75 ± 3	178.4
60Zn	39 ± 6	16.1	0.16	39.2	41 ± 3	67 ± 3	135.6
90Zn	53 ± 5	7.3	0.056	30.7	35 ± 2	60 ± 1	101.2
100Zn					31 ± 2	52 ± 3	

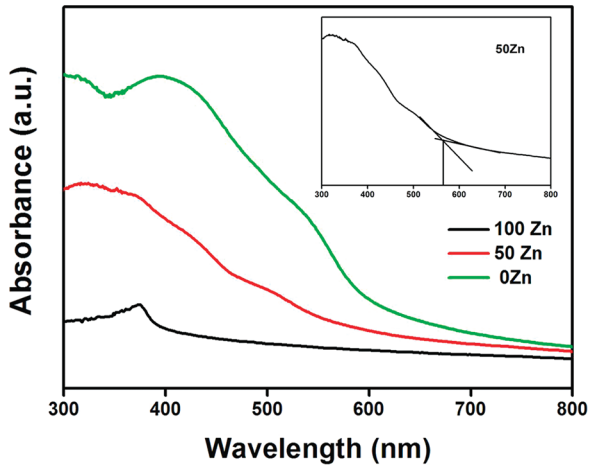

Figure 3. UV−vis spectrum of 100Zn, 0Zn, and 50Zn samples. Inset shows the band gap calculation of 50Zn.

100Zn and the property of $ZnFe_2O_4$ as it contains 52 %. This also suggests the strong interaction between Fe and Zn in 50Zn sample, and is well tallied with the XRD result.

3.5. XPS. XPS was carried out to establish the electronic environment and oxidation state of the elements those are present in the studying system. All the core level spectra of characteristic elements were represented in Figure 4a−c. There is appearance of two binding energy (BE) peaks for core-level spectra of O 1s. The low BE component observed at 529.2 eV is attributed to the O^{2-} forming oxide whereas the later one appeared at 530.7 eV is assigned to OH^-.[2] The peak position of Fe $2p_{3/2}$ for α-Fe_2O_3 has been investigated by many researchers previously, who have reported that the value of binding energy (BE) lies between 710.6 and 711.2 eV.[36−39] In our sample, the BE of Fe $2p_{3/2}$ and $2p_{1/2}$ were observed at 710.8 and 724.4 eV, respectively which confirms the +3 oxidation state of iron. Similarly, ZnO exhibits its $2p_{3/2}$ peak at 1021.7.[36,40] However, the present sample gives its BE peaks at 1021($2p_{1/2}$) and 1043.99 ($2p_{3/2}$) because of the +2 oxidation state. As evidenced from the XPS observation, both the Zn^{2+} and Fe^{3+} are in oxide form rather than in metallic form.

3.6. N_2 Adsorption−Desorption Isotherm. The surface area of the catalysts was measured from BET analysis, which played a vital role in photocatalysis. Generally higher surface area is favorable for photocatalytic activity due to more number of active sites available for photocatalytic reaction.[41] The BET surface area, pore volume and pore diameter of all the catalysts were presented in Table 1. In the present investigation the surface area of the photocatalysts are varied in the region of 7 to 18 m^2/g. Among all prepared photocatalysts, the BET surface area of 50Zn catalyst is maximum and found to be 17.7 m^2/g, which plays a pivotal role for good photocatalytic activity. The pore volume and average pore diameter were found to be 0.17 cm^3/g and 43.8 nm, respectively.

3.7. AAS Study. The leachability of the metal contents of 50Zn sample during the photocatalytic reaction was analyzed by AAS study. No significant loss of both Fe and Zn were observed after the photocatalytic reaction. The content of iron and zinc before and after the photocatalytic reaction were found to be 41.2, 19.8, and 40.7 and 19 %, respectively.

3.8. Photoelectrochemical Measurement. To examine the nature of photoelectric behaviour of 50Zn sample, photoelectrochemical measurements were carried out by using its film prepared as photoelectrode. Figure 5 shows the current−potential relationship for 50Zn electrodes under chopped visible light irradiation (λ > 400 nm). The photoelectrochemical measurement was carried out in 0.1M Na_2SO_4 solution with pH maintaining at 4.2 by H_2SO_4. From the current−potential diagram, the photocurrent becomes anodic, under visible light illumination and increases in magnitude in the positive direction. It was clearly observed that the electrode generates anodic photocurrent with applied bias. This result indicates that the prepared photoelectrode has n-type semiconducting character.

3.9. Photoresponse Spectra. The dependence of initial photocurrent with the wavelength of incident light is shown in Figure 6. These data were obtained by irradiating samples via appropriate cut-off filters for the wavelength shown with the current generated from the photoelectrode. Figure 6 clearly showed the absorbance of the photocatalyst decreases with increasing the wavelength. As in the figure, it was observed that the generation of photocurrent decreases with the increase of wavelength. There was also no photocurrent observed longer than 610 nm when the sample was irradiated at wavelength, which is consistent with the absorption edge shown in Figure 6. This indicates that the photocurrent generated by the 50Zn sample is due to the band gap excitation of the photocatalysts.

3.10. Photocatalytic Reaction. Here we have discussed the photocatalytic activity of the synthesized catalyst and explained it briefly. The photocatalytic reactions have been categorized into two parts.

3.10.1. Photo-fenton Reaction. The percentage of degradation of CNP and R6G were investigated as a function of different catalysts. Previously we have studied CNP degradation over N-doped GaZn mixed oxide under visible light irradiation and the degradation was found to be 54%.[42] Dukkanc et al. reported the photo-fenton reaction over CuFeZSM-5 zeolite catalyst. They have performed the reaction at 50 °C and got 100 % R6G degradation.[9] In the present investigation, 50Zn showed excellent activity among all the synthesized samples

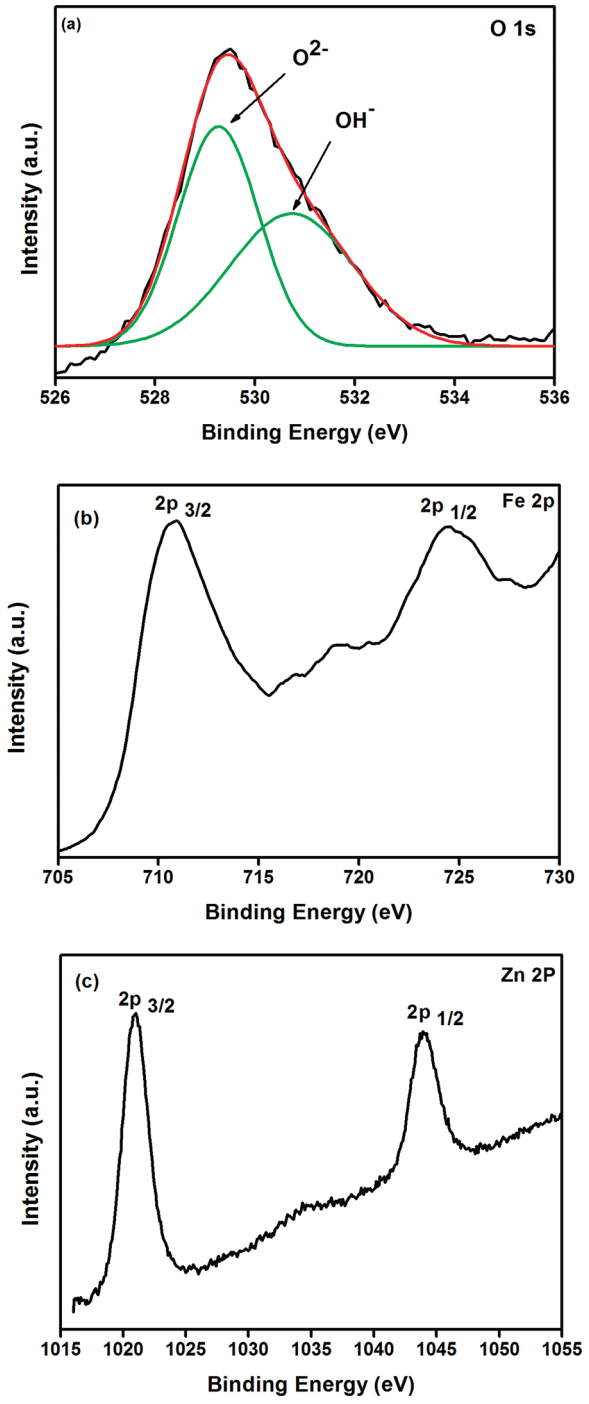

Figure 4. XPS spectrum of 50Zn photocatalyst : (a) high-energy-resolution O 1s core-level spectra, (b) high-energy-resolution Fe 2p core-level spectra and (c) high-energy-resolution Zn 2p core-level spectra.

towards degradation of CNP and R6G. The photocatalyst could be able to degrade 56% and 75% of CNP and R6G (100 mg/L), respectively under direct solar light irradiation in just 4 h. But both pure and lower content of iron and zinc showed lowest degradation activity. The photo degradation was summarized in Table 1. TOC was performed to know how much percentage of organic carbon converted to CO_2 during the photocatalytic reaction. The calculated TOC removal for CNP and R6G over 50Zn were found to be 37 and 44 %, respectively, after photocatalytic reaction.

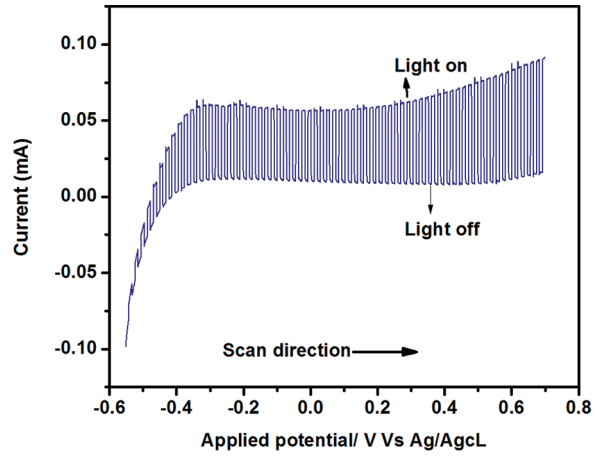

Figure 5. Current−potential curves of 50 Zn sample with $\lambda \geq 400$ nm.

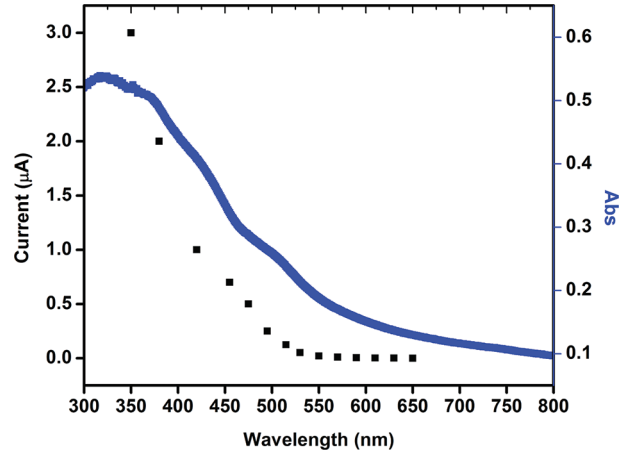

Figure 6. Dependence of photocurrent of 50 Zn sample on irradiation wavelength (dotted line). DRUV−vis spectrum is also shown in solid line.

3.10.2. Photocatalytic Hydrogen Generation. Photocatalytic H_2 production over 50Zn oxide was evaluated. Blank experiments showed no appreciable H_2 production in the absence of either irradiation or photocatalyst. The amount of hydrogen gas evolved over 50Zn under visible light irradiation using 10 vol% methanol solution as sacrificial agent are shown in Table 1. Highest amount of H_2 gas evolved over the 50Zn was observed to be 178.4 μmol/h (Figure 7). The photocatalysts could be able to evolve 786 μmol in initial 5 h of photocatalytic reaction. It is clearly observed from the Figure 8 that the activity of the photocatalysts remain almost unchanged in the repeated runs which determined the stability of the photocatalyst. When the reaction was carried out in aqueous solutions including easily oxidizable reducing agents, i.e., methanol, the photogenerated holes irreversibly oxidizes methanol instead of water. This makes the photocatalyst rich with electrons which enhances the hydrogen evolution process (Scheme 5b).[43]

3.10.3. Mechanism of Photodegradation. There are two mechanisms for the photodegradation. The hydroxyl radical is generated in two ways. First one is photolysis (Scheme 3 and Scheme 5a), where as second one is photofenton (Scheme 4).[44−46] In photolysis, when the photocatalyst was exposed to sunlight, an electron jumps from the valence band to the conduction band creating a hole in the valence band. The

dx.doi.org/10.1021/am201326b | ACS Appl. Mater. Interfaces 2012, 4, 707−713

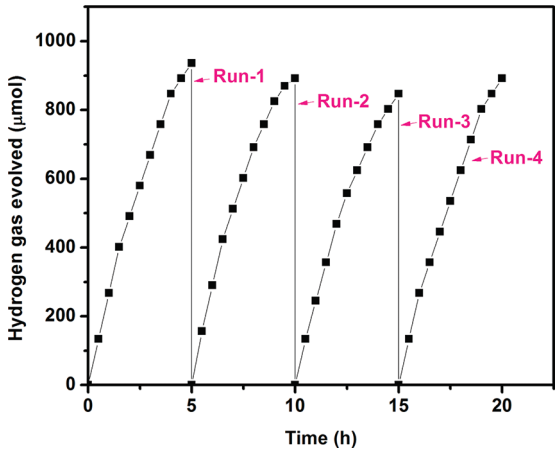

Figure 7. H_2 evolution over 50 Zn under visible light illumination ($\lambda \geq$ 400 nm).

Scheme 3. Mechanism of Formation of Hydroxyl Radical by Photolysis, FZ Denotes Iron–Zinc Nano Mixed Oxide Photocatalyst

$$FZ + h\nu \longrightarrow FZ + e^- + h^+ \quad (1)$$

$$OH^- + h^+ \longrightarrow OH^{\bullet} \quad (2)$$

$$O_2 + e^- \longrightarrow O_2^{\bullet -} \quad (3)$$

$$O_2^{\bullet -} + H^+ \longrightarrow HO_2^{\bullet} \quad (4)$$

$$2HO_2^{\bullet} \longrightarrow H_2O_2 + O_2 \quad (5)$$

$$H_2O_2 + e^- \longrightarrow OH^{\bullet} + OH^- \quad (6)$$

Scheme 4. Mechanism of Formation Perhydroxyl and Hydroxyl Radicals by Photofenton Reaction

$$Fe^{3+} + H_2O_2 \longrightarrow [Fe^{III}OOH]^{2+} + H^+ \quad (7)$$

$$[Fe^{III}OOH]^{2+} \longrightarrow Fe^{2+} + OOH^{\bullet} \quad (8)$$

$$[Fe^{III}OOH]^{2+} \longrightarrow [Fe^{IV}O]^{2+} + OH^{\bullet} \quad (9)$$

$$[Fe^{III}OOH]^{2+} \longrightarrow [Fe^{V}O]^{3+} + OH^- \quad (10)$$

$$Fe^{2+} + H_2O_2 \longrightarrow Fe^{3+} + OH^{\bullet} + OH^- \quad (11)$$

$$Fe^{2+} + H_2O_2 \longrightarrow [Fe^{IV}O]^{2+} + H_2O \quad (12)$$

photogenerated hole interacts with the surface hydroxyl group present on the surface of the catalyst to generate the hydroxyl radical. On the otherhand the photogenerated electron in the conduction band react with the dissolved oxygen forming superoxide, which again intermingles with the proton, yielding the hydroperoxyl radical followed by the formation of hydrogen peroxide. Then hydroxyl radical is produced by the attack of photogenerated electron to the hydrogen peroxide. In photo-fenton reaction, the production of highly reactive perhydroxyl and hydroxyl radicals (steps 8, 9) is responsible for the degradation of organic pollutants. Some authors claim that Fe^{3+} species are responsible for the formation of various active intermediates to produce perhydroxyl and hydroxyl radicals.[45] The reduced species (Fe^{2+}) again interact with H_2O_2 to produce hydroxyl radical (step 11).

Several factors have been discussed that explain the superior catalytic activity of 50Zn sample. Among all the developed photocatalysts, 50Zn showed excellent photocatalytic activity towards photocatalytic degradation of CNP and R6G and towards hydrogen evolution reaction as well. Generally, higher surface area is favorable for photocatalytic reaction. In the present investigation, the surface area is varied in the region of 7–18 m^2/g. The photocatalysts prepared at the ratio of 50:50 (50Zn) showed higher surface area of 17.8 m^2/g. So larger number of active sites are available for photocatalytic reaction, which results in higher photocatalytic activity. In the case of both pure and lower content of iron and zinc, the degradation was lower. Electron-hole recombination predominates in case of higher iron content where as lower absorptivity prevails on higher zinc content. On increasing the content of zinc and iron, the degradation was also increased and the optimum results were obtained at their equal percentage (50Zn). The prepared 50 Zn might be retarding the recombination of photoinduced charge carriers to a great extent which might be one of the causes of best activity of the prepared photocatalysts. At the interface of 50Zn photocatalyst, the electron-hole separation might be promoted (Scheme-3) which enhances the photo-catalytic activity.[43] The results of 50Zn photocatalyst was also compared with phase pure $ZnFe_2O_4$. But it was found to be less active than 50Zn where all the three phases viz. $ZnFe_2O_4$, Fe_2O_3, and ZnO were present. The highest activity showed by sample 50Zn may be due to synergism between $ZnFe_2O_4$, Fe_2O_3, and ZnO. From DRS study, the bandgap energy of 50Zn (2.19 eV) also supports the high absorptive power in the visible range and lower electron hole recombination compared to 100Zn (3.19 eV) and 0Zn (2.0 eV). At the interface of ZnO and Fe_2O_3 crystallites, the Fermi energy levels of the two materials have to be the same. This leads both conduction band and valence band of Fe_2O_3 lie above the ZnO. This results in gathering of large number of electrons on the conduction band of ZnO surface and holes on the valence band of Fe_2O_3. This enhances the separation of free charge carriers. Thus the presence of large number of free electrons and holes are mostly responsible for high photocatalytic activity.

Scheme 5. Schematic Representation of (a) Photocatalytic Dye Degradation (b) Photocatalytic H_2 Production

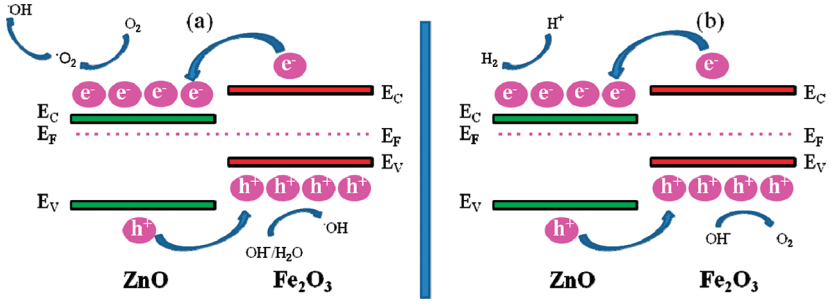

dx.doi.org/10.1021/am201326b | ACS Appl. Mater. Interfaces 2012, 4, 707–713

3.10. Reusability. To determine the stability of the catalyst, we performed reusability studies over 50Zn. The photocatalyst was tested for three times in presence of H_2O_2 under solar light irradiation. After each cycle, the catalyst was washed with ethanol and dried at 110 °C to remove any surface contamination. A slight decrease in the degradation of both R6G and CNP was observed over 50Zn photocatalyst. After three cycles, the degradation of CNP and R6G over 50Zn was found to be 49 and 71%, respectively.

4. CONCLUSIONS

We have successfully fabricated the iron−zinc nano mixed oxide by a simple solution-combustion technique. The formation of mixed oxide was evident from both XRD and XPS. The photocurrent measurement showed that the prepared photocatalysts are of n type semiconductor. The multifunctional behaviour of the prepared photocatalysts were successfully examined towards degradation of CNP, R6G and photocatalytic hydrogen generation under visible light. The best photocatalyst having Zn:Fe molar ratio of 50:50 (50Zn) shows a degradation of 56 and 72 % of CNP and R6G, respectively, and hydrogen production of 178.4 μmol/h.

AUTHOR INFORMATION

Corresponding Author

*E-mail: paridakulamani@yahoo.com. Fax: 91674-2581637.

ACKNOWLEDGMENTS

The authors are extremely thankful to Prof. B.K. Mishra, Director, IMMT, Bhubaneswar, for his constant encouragement and permission to publish the paper. We are also very grateful to CSIR for providing SRF fellowship to Mr. G. K. Pradhan.

REFERENCES

(1) Linsebigler, A. L.; Lu, G. Q.; Yates, J. T. *Chem. Rev.* **1995**, *95*, 735.
(2) Pradhan, G. K.; Parida, K. M. *ACS Appl. Mater. Interfaces* **2011**, *3*, 317−323.
(3) Fujishima, A.; Honda, K. *Nature* **1972**, *238*, 37−38.
(4) Cowan, A. J.; Tang, J.; Leng, W.; Durrant, J. R.; Klug, D. R. *J. Phys. Chem. C* **2010**, *114*, 4208−4214.
(5) Kato, H.; Asakura, K.; Kudo, A. *J. Am. Chem. Soc.* **2003**, *125*, 3082−3089.
(6) Siritanaratkul, B.; Maeda, K.; Hisatomi, T.; Domen, K. *ChemSusChem* **2011**, *4*, 74−78.
(7) Maeda, K.; Abe, R.; Domen, K. *J. Phys. Chem. C* **2011**, *115*, 3057−3064.
(8) Yunus, R. F.; Zheng, Y. M.; Nanayakkara, K. G. N.; Chen, J. P. *Ind. Eng. Chem. Res.* **2009**, *48*, 7466−7473.
(9) Dükkancı, M.; Gündüza, G.; Yılmazb, S.; Prihodko, R.V. *J. Haz. Mater* **2010**, *181*, 343−350.
(10) Roostaei, N.; Tezel, F. H. *J. Environ. Manage.* **2004**, *70*, 157.
(11) Greca, M. D.; Monaco, P.; Pinto, G. *Bull. Environ.Contam. Toxicol.* **2001**, *67*, 352.
(12) Garg, R.; Kapur, S.; Hansch, C. *Med. Res. Rev.* **2001**, *21*, 28.
(13) Gupta, V. K.; Ali, I.; Saini, V. K. *Environ. Sci. Technol.* **2004**, *38*, 4012.
(14) Beltran, F. J.; Serrano, V. G.; Duran, A. *Water Res.* **1992**, *26*, 9.
(15) Chow, Y. L.; Patai, S. *Chemistry of Functional Groups Series*; J. Wiley & Sons: Chichester, U.K., 1982.
(16) Balcioglu, I. A.; Inel, Y. *Environ. Sci. Health.* **1996**, *31*, 123.
(17) Cesar, I.; Kay, A.; Martinez, J. A. G.; Gratzel, M. *J. Am. Chem. Soc.* **2006**, *128*, 4582.
(18) Luo, W.; Wang, D.; Wang, F.; Liu, T.; Cai, J.; Zhang, L.; Liu, Y. *Appl. Phys. Lett.* **2009**, *94*, 202507.
(19) Hu, Y. S.; Shwarsctein, A. K.; Forman, A. J.; Hazen, D.; Park, J. N.; McFarland, E. W. *Chem. Mater.* **2008**, *20*, 3803.
(20) Aroutiounian, V. M.; Arakelyan, V. M.; Shahnazaryan, G. E.; Stepanyan, G. M.; Turner, J. A.; Khaselev, O. *Inter. J. Hydrogen Energy* **2002**, *27*, 33.
(21) Vayssies, L.; Sathe, C.; Butorin, S. M.; Shuh, D. K.; Nordgren, J.; Guo, J. *Adv. Mater.* **2005**, *17*, 2320.
(22) Shet, S.; Ahn, K. S.; Deutsch, T.; Wang, H.; Ravindra, N.; Yan, Y.; Turner, J.; Jassim, M. A. *J. Mater. Res.* **2010**, *25*, 69−75.
(23) Jang, J. S.; Choi, S. H.; Kim, H. G.; Lee, J. S. *J. Phys. Chem. C.* **2008**, *112*, 17200−17205.
(24) Shvalagin, V. V.; Stroyuk, A. L.; Kotenko, I. E.; Kuchmii, S. Y. *Theor. Exp. Chem.* **2007**, *43*, 229−234.
(25) Liu, Z.; Sun, D. D.; Guo, P.; Leckie, J. O. *Nano Lett.* **2007**, *7*, 1081−1085.
(26) Kim, J. Y.; Choi, S. B.; Noh, J. H.; Yoon, S. H.; Lee, S.; Noh, T. H.; Frank, A. J.; Hong, K. S. *Langmuir* **2009**, *25*, 5348−5351.
(27) Suber, L.; Imperatori, P.; Ausanio, G.; Fabbri, F.; Hofmeister, H. *J. Phys. Chem. B* **2005**, *109*, 7103−7109.
(28) An, Z.; Zhang, J.; Pan, S.; Yu, F. *J. Phys. Chem. C* **2009**, *113*, 8092−8096.
(29) Parviz, D.; Kazemeini, M.; Rashidi, A. M.; Jozani, K. J. *J. Nanopart. Res.* **2010**, *12*, 1509−1521.
(30) Toniolo, J.; Takimi, A. S.; Andrade, M. J.; Bonadiman, R.; Bergmann, C. P. *J. Mater. Sci.* **2007**, *42*, 4785−4791.
(31) Murugan, B.; Ramaswamy, A. V. *Chem. Mater.* **2005**, *17*, 3983−3993.
(32) Naik, B.; Parida, K. M.; Gopinath, C. S. *J. Phys. Chem. C* **2010**, *114*, 19473−19482.
(33) Mapa, M.; Sivaranjani, K.; Bhange, D. S.; Saha, B.; Chakraborty, P.; Viswanath, A. K.; Gopinath, C. S. *Chem. Mater.* **2010**, *22*, 565−578.
(34) Giordano, C.; Erpen, C.; Yao, W.; Mike, B.; Antonietti, M. *Chem. Mater.* **2009**, *21*, 5136−5144.
(35) Cornell, R. M.; Schwertmann, U. *The Iron Oxide Book*; 2nd ed.; Wiley−VCH: Weinheim, Germany, 2003; p 147.
(36) Wagner, C. D.; Riggs, W. M.; Davis, L. E.; Muilenberg, J. F. *Handbook of X-ray Photoelectron Spectroscopy*; Perkin Elmer: Eden Prairie, MN, 1979.
(37) Bhargaba, G.; Gouzman, I.; Chun, C. M.; Ramanarayanan, T. A.; Bernasek, S. L. *Appl. Surf. Sci.* **2007**, *253*, 4322−4329.
(38) Yamashita, T.; Hayes, P. *Appl. Surf. Sci.* **2008**, *254*, 2441−2449.
(39) Grosvenor, A. P.; Kobe, B. A.; Biesinger, M. C.; Mclntyre, N. S. *Surf. Inter. Anal.* **2004**, *36*, 1564−1574.
(40) Lee, C. Y.; Tseng, T. Y.; Li, S. Y.; Lin, P. *Tamkang J. Sci. Eng.* **2003**, *6*, 127−132.
(41) Parida, K. M.; Reddy, K. H.; Martha, S.; Das, D. P.; Biswal, N. *Int. J. Hydrogen Energy* **2010**, *35*, 12161−12168.
(42) Martha, S.; Reddy, K.; Parida, K. M.; Satapathy, P. K. *Int. J. Hydrogen Energy* **2012**, *37*, 115−124.
(43) Parida, K. M.; Martha, S.; Das, D. P.; Biswal, N. *J. Mater.Chem.* **2010**, *20*, 7144−7149.
(44) Pradhan, G. K.; Parida, K. M. *Int. J. Eng. Sci. Technol.* **2010**, *2*, 53−65.
(45) Gokulakrishnan, N.; Pandurangan, A.; Sinha, P. K. *Ind. Eng. Chem. Res.* **2009**, *48*, 1556−1561.
(46) Niu, M.; Huang, F.; Cui, L.; Huang, P.; Yu, Y.; Wang, Y. *ACS Nano* **2010**, *4*, 681−688.